ISSN (Print) 1226-1750
ISSN (Online) 2233-6656
Journal of Magnetics 31(2), 165-177 (2026) https://doi.org/10.4283/JMAG.2026.31.2.165

Design and Analysis of Modular Concentrated Winding Permanent Magnet Generator with Reduced Short-Circuit Current

Lin Zhang[1], Yuhua Sun[2]*, Yu Nan[1], Weiping Niu[1], Wenxiang Zhao[2], Yuxuan Du[2], and Xindi Wang[2]

[1]*Kaifeng Power Supply Company, State Grid Henan Electric Power Company, Kaifeng 450052, Henan Province, China*
[2]*School of Electric Power Engineering, Nanjing Institute of Technology, Nanjing 211167, Jiangsu Province, China*

(Received 2 April 2026, Received in final form 6 June 2026, Accepted 15 June 2026)

Permanent magnet generators (PMG) have garnered widespread attention in the wind power generation application owing to their high efficiency and large torque density. Meanwhile, the drawback of large short-circuit current has become a key bottleneck restricting the performance improvement. Taking 18-slot/16-pole and 24-slot/22-pole fractional-slot concentrated winding PMG as the research objects, a modular concentrated winding structure based on stator tooth offset was proposed to achieve the coordinated design of low short-circuit current and high average torque. Firstly, the structural characteristics of modular concentrated winding were discussed, the evolution law between the original and modular structures was explored, and the design principles of modular concentrated windings with stator tooth offset were summarized. Secondly, the modulation effects of the original and modular structures on the air-gap magnetic field were analyzed, and the variation characteristics of the permanent magnet and armature magnetic field harmonics under different structures were compared. Then, the torque, inductance, and short-circuit current performances with different slot/pole combinations adopting the original and modular structures were compared, revealing the effectiveness of the modular concentrated winding structure in improving the average torque and suppressing the short-circuit current. Finally, the 18-slot/16-pole PMG adopting the original and modular structures were manufactured respectively, and a test platform was built for experimental verification.

Keywords : permanent magnet generator, modular structure, stator tooth offset, short-circuit current, torque

1. Introduction

Driven by both global energy transition and environmental protection, the efficient development and utilization of renewable energy have become an important component of global energy strategies [1]. Under this development trend, the advantages of widespread distribution and abundant reserves of wind energy resources are becoming increasingly prominent, making wind power generation an important direction for the development of renewable energy [2].

As the key component for energy conversion in wind turbine systems, generators commonly include doubly-fed induction generator and permanent magnet generator (PMG) [3, 4]. Doubly-fed induction generators rely on slip rings and brushes, which are prone to malfunctions due to brush wear and poor contact [5]. In contrast, PMGs do not require excitation windings and possess advantages such as high efficiency and reliable operation [6-8]. Moreover, it demonstrates grid-friendly characteristics through grid connection via a full-power converter. Wind generators operate in the open air at high altitudes for extended periods, facing harsh environmental conditions. As the operational airspace and speed range of PMGs continue to expand, they are highly susceptible to faults such as inter-turn short-circuits in the windings. This can lead to severe short-circuit current (SCC), causing coil overheating and irreversible demagnetization of PM [9]. The safety of the power generation system is seriously threatened.

The SCC suppression is key to improving the fault-tolerant operation capability of PMG. The permanent magnet flux linkage and winding impedance are crucial parameters that determine the SCC characteristics [10-12]. Since permanent magnet flux linkage directly determines torque capability, high-impedance design has become the principal approach for designing PMGs with low SCC. Closed stator slots or magnetic slot wedge

*Corresponding author: Tel: +86-15751017179
e-mail: 1714034249@qq.com

structures have been widely applied for SCC suppression [13]. However, these methods increase leakage flux, reduce the power factor, and consequently lower the torque output. In [14], the influence of dimensional parameters on SCC was investigated. The results indicate that the SCC can be reduced by reducing the permanent magnet pole arc coefficient, stator slot opening width, and rotor yoke thickness, or increasing the stator tooth tip height. In addition, as the inner-to-outer diameter ratio and stator tooth width increase, the SCC first rises and then falls. It should be noted that the effectiveness of SCC suppression is highly sensitive to the dimension accuracy, and typically entails a reduction in average torque. The auxiliary teeth inside the stator slot structure were proposed in [15]. This can increase inductance to reduce SCC while also enabling short-circuit fault diagnosis through changes in flux paths before and after the fault. However, this structure inevitably sacrifices the effective stator slot area and increases copper loss. In [16], an E-core stator structure was adopted to suppress SCC by introducing flux barriers at the center of stator teeth. However, it intensifies stator tooth saturation and reduces average torque. Moreover, this structure cannot be applied when the slot number is smaller than the pole number. In summary, existing SCC suppression methods are unable to achieve a coordinated design of low SCC and high torque in PMGs [17-19].

This paper proposes a modular fractional slot concentrated winding PMG based on stator tooth offset for SCC suppression. The phase windings exhibit obvious modular spatial distribution characteristics, the SCC is significantly suppressed, and the average torque is improved. Firstly, the design method of the modular concentrated winding structure was investigated, with emphasis on the evolution law from the original structure to the modular structure. Secondly, the effects of the modular structure on the permanent magnet field and armature field were analyzed in depth, and the variations of the fundamental harmonic amplitudes under different structures were compared. Then, the influence of the modular structure on electromagnetic performances was discussed from the perspectives of torque, inductance, and SCC. The effectiveness of the proposed modular structure in simultaneously improving average torque and reducing SCC was revealed. Finally, two 18-slot/16-pole PMGs with original and modular structures were prototyped and experiments were carried out for validation.

2. Modular Concentrated Winding Design

Fig. 1 shows the cross section of the 18-slot/16-pole

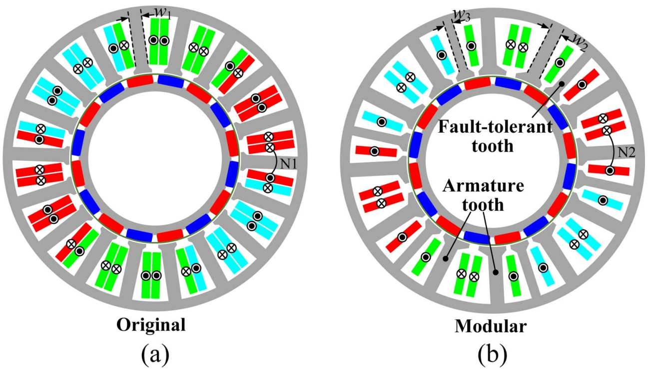

Fig. 1. (Color online) Cross section of the 18-slot/16-pole PMG. (a) Original. (b) Modular.

PMGs with different stator structures. For both rotors, a surface-mounted structure is adopted and they have identical dimensions, while the original structure and the modular structure are employed for the stators, respectively. The original structure is a double-layer fractional-slot concentrated winding structure, in which the stator armature teeth are evenly distributed. The stator tooth width is w_1, the slot pitch angle is 20°, the stator slot area is S_1, and the number of turns per coil is N_1. Three coils are continuously and concentrically distributed, which inevitably causes the fact that coils of different phases are distributed in the same stator slot. Therefore, the risk of fault propagation is increased after the occurrence of winding fault. In contrast, a mixed single and double-layer concentrated winding structure is adopted for the modular structure. The design process of the modular structure can be divided into three steps. Firstly, the stator is divided equally along the air-gap circumference into six modules based on the spatial distribution of each phase winding. Secondly, to avoid windings of different phases appearing in the same stator slot, one coil is removed from each module. Since each module has three stator teeth and two coils, there is one stator tooth that is not wound. Therefore, the stator teeth of each module are divided into two armature teeth and one fault-tolerant tooth. The fault-tolerant tooth serves to separate coils belonging to different phase windings. Thirdly, the shifting angle between the armature teeth increases from 20° to 22.5°, and the width of armature and fault-tolerant teeth are optimized while maintaining the proportional relationship of slot areas. Therefore, in the modular structure, the number of coils in each phase winding is reduced to 2/3 of that in the original structure. The number of turns per coil becomes N_2=1.5N_1. Fig. 2 shows the winding connection diagrams of the 18-slot/16-pole PMG with different stator structures. The coils of each

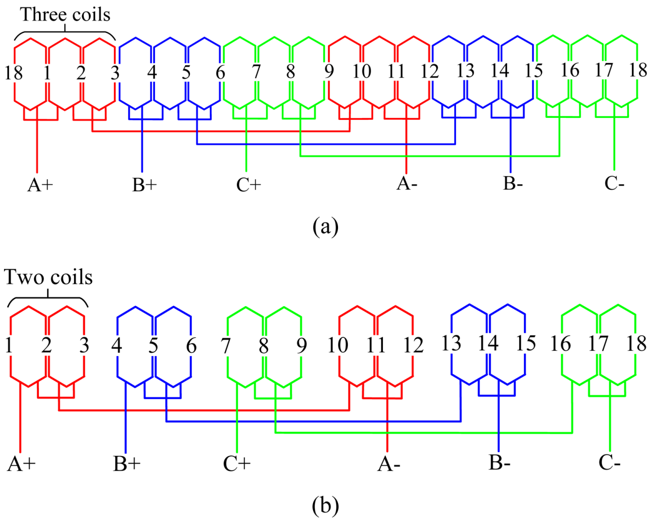

Fig. 2. (Color online) Winding connection diagram of the 18-slot/16-pole PMG. (a) Original. (b) Modular.

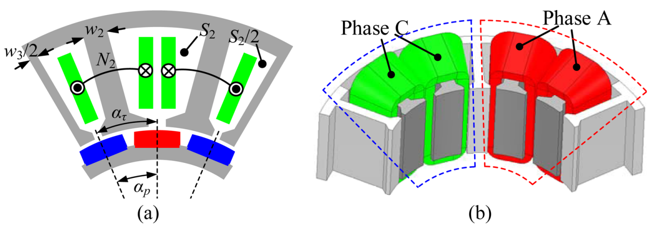

Fig. 3. (Color online) Partial view of the 18-slot/16-pole PMG with modular structure. (a) 2D. (b) 3D.

phase are independently distributed in one stator module and spatially isolated from one another, greatly improving the inter-phase independence.

Fig. 3 presents a local view of the modular stator structure to clearly illustrate the structural characteristics, where α_τ denotes the coil pitch angle in the modular structure and α_p denotes the pole pitch. Based on the stator tooth offset technique, full-pitch windings are adopted for the modular structure, namely, $\alpha_\tau=\alpha_p=22.5°$. Furthermore, the widths of the armature tooth and fault-tolerant tooth in the modular structure are w_2 and w_3, respectively. To ensure that the phase resistances of the original and modular structures are identical, the total slot area of the two structures is kept the same. Therefore, in the modular structure, the slot area for the double-layer winding is $S_2=1.5S_1$, while the slot area for the single-layer winding is $S_2/2$. Under the constraint of the above slot area, the stator tooth widths in the original and modular structures must satisfy the following dimensional constraint.

$$3w_1 = 2w_2 + w_3 \tag{1}$$

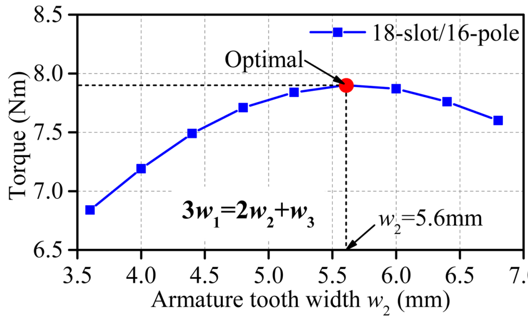

Fig. 4. (Color online) Torque variation with tooth width for the 18-slot/16-pole PMG with modular structure.

Fig. 4 shows the torque variation of the modular structure of the 18-slot/16-pole PMG with changing tooth widths. On this basis, the armature tooth width of the modular stator structure is determined as w_2=5.6 mm, while the fault-tolerant tooth width is w_3=3.8 mm.

In addition, the design method of the modular stator structure can be extended to other slot/pole combinations. Fig. 5 shows the cross section of the 24-slot/22-pole PMGs in which the original and modular stator structures are employed, respectively. The modular structure divides the stator equally into six modules along the air-gap circumference as well. Each module consists of three armature teeth and one fault-tolerant tooth. Fig. 6 shows the local view of the 24-slot/22-pole PMG with modular stator structure, where the fault-tolerant tooth spatially

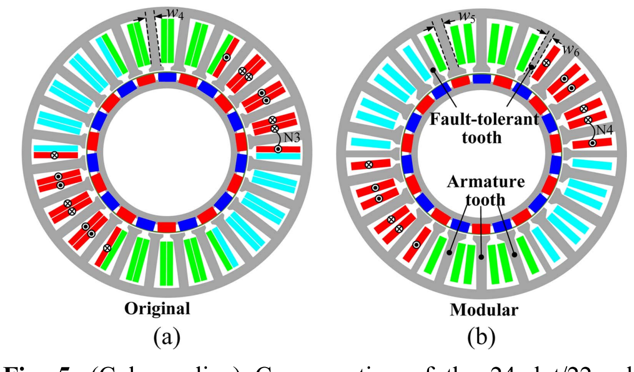

Fig. 5. (Color online) Cross section of the 24-slot/22-pole PMG. (a) Original. (b) Modular.

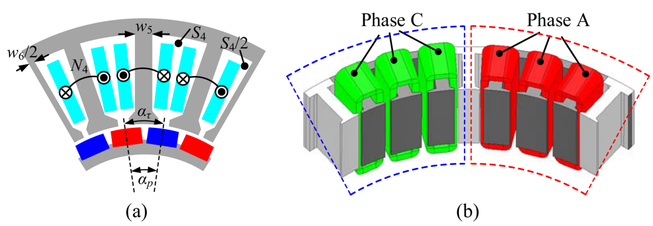

Fig. 6. (Color online) Partial view of the 24-slot/22-pole PMG with modular structure. (a) 2D. (b) 3D.

separates the phase windings. In the original structure, the stator tooth width is w_4, the stator slot area is S_3, and the number of turns per coil is N_3. In contrast, in the modular structure, the number of coils in each phase is reduced to 3/4 of that in the original structure, and the number of turns per coil becomes N_4=1.3N_3. The slot area for the double-layer winding is S_4=1.3S_3, and that for the single-layer winding is S_4/2. Under the slot-area constraint described above, the stator tooth widths of the original and modular structures in the 24-slot/22-pole PMG must satisfy the following dimensional relation.

$$4w_4 = 3w_5 + w_6 \tag{2}$$

In summary, the modular stator structure has the following characteristics:

a) The stator exhibits obvious modular distribution characteristics. The coils in each stator module belong to the same phase, and each module contains one fault-tolerant tooth that separates different phase windings.

b) In the original structure, short-pitch windings are adopted, whereas full-pitch windings are adopted in the modular structure; that is, the tooth-slot pitch angle of the modular structure is equal to the pole pitch angle.

c) The total number of series turns per phase is identical in the original and modular structures. Thus, in the modular structure, the number of coils is reduced while the turns per coil are increased.

d) The total stator slot area is the same for the original and modular structures.

Based on the above structural features, Table 1 gives the dimensional parameters of the 18-slot/16-pole and 24-slot/22-pole permanent magnet generators.

Table 1. Structure parameters of the PMGs with different slot/pole combinations.

Items	18-slot/16-pole		24-slot/22-pole	
	Original	Modular	Original	Modular
Rotor speed (r/min)	2000		2000	
Rated phase current (A)	7		7	
Stator outer diameter (mm)	120		120	
Stator inner diameter(mm)	68		68	
Axial length (mm)	50		50	
Turn number per coil	40	60	30	40
Slot area (mm^2)	233	350/175	172	230/115
Stator tooth width (mm)	5.0	5.6/3.8	3.7	4.1/2.5
Slot pitch angle (°)	20	22.5	15	16.4
Phase resistance (Ω)	0.63		0.58	
Rotor inner diameter (mm)	30		30	
PM thickness (mm)	4		4	

3. Magnetic Field Analysis

3.1. Permanent Magnet Field

This section compares the effects of the original and modular structures on the permanent magnet field of the machine. The permanent magnet field can be expressed as:

$$B_{\mathrm{PMs}}(\theta_m,\Omega_r t) = B_{\mathrm{PM}}(\theta_m,\Omega_r t)\cdot\Lambda_s(\theta_m) \tag{3}$$

where

$$\begin{cases} B_{\mathrm{PM}}(\theta_m,\Omega_r t) = \sum\limits_{k=1,3,5...} B_k\cos\left[kp\left(\theta_m-\Omega_r t\right)+\varphi_k\right] \\ \Lambda_s(\theta_m) = \Lambda_{s0}+\sum\limits_{n.}^{\infty}\Lambda_{sn}\cos\left(n\theta_m\right) \end{cases}$$

where B_{PM} denotes the primitive permanent magnet field without considering the stator structure, and Λ_s denotes the permeance function after stator slotting. θ_m denotes the rotor position in the stator coordinate system, p is the number of pole pairs, Ω_r is the mechanical angular velocity, and B_k and φ_k are the amplitude and phase of the kp^{th}-order harmonic of the primitive permanent magnet field, respectively. Since the rotor dimensions are identical in the original and modular structures, both machines have the same primitive permanent magnet field. Λ_{s0} and Λ_{sn} denote the average and the n^{th}-order harmonic amplitude of the stator permeance function, respectively. For the original structure, n is an integer multiple of the slot number, whereas n is an integer multiple of the module number for the modular structure. Considering the effect of stator slotting on the permanent magnet field, the harmonic order of the permanent magnet flux density in the air gap can be expressed as $|kp\pm n|$. Taking the 18-slot/16-pole PMG as an example, the harmonic components of the primitive permanent magnet field are the 8$^{\mathrm{th}}$, 24$^{\mathrm{th}}$, 40$^{\mathrm{th}}$, etc. The first-order permeance harmonic of the original structure is the 18$^{\mathrm{th}}$-order, whereas that of the

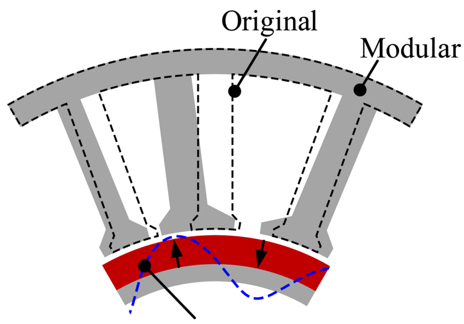

Fig. 7. (Color online) Finite element model of sinusoidal magnetization for the 18-slot/16-pole PMG.

modular structure is the 6th-order.

To compare the influence of different stator structures on the permanent magnet field, the 18-slot/16-pole PMG is taken as an example. Fig. 7 establishes a finite-element model with sinusoidally magnetized permanent magnets, in which the primitive permanent magnet field contains only the 8th-order fundamental component. New harmonic components emerge due to the stator slotting. Specifically, when the original stator structure is adopted, the 10th-, 26th-, and 28th-order harmonic components are generated. When the modular stator structure is adopted, the 4th-, 12th-, 14th-, 16th-, 20th-, and 22th-order harmonic components appear. In other words, the modular structure increases the harmonic components of the permanent magnet field, as shown in Fig. 8. The stator slot opening widths are the same in both structures. Therefore, the average value of the stator permeance function Λ_{s0} is similar. The modular structure does not reduce the fundamental component of the permanent magnet field.

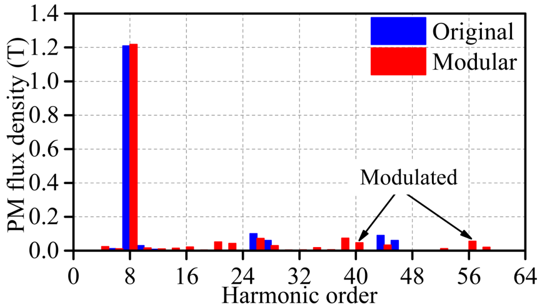

Fig. 8. (Color online) Modulation effect of the modular structure of the 18-slot/16-pole PMG on the 8th-order fundamental PM magnetic field.

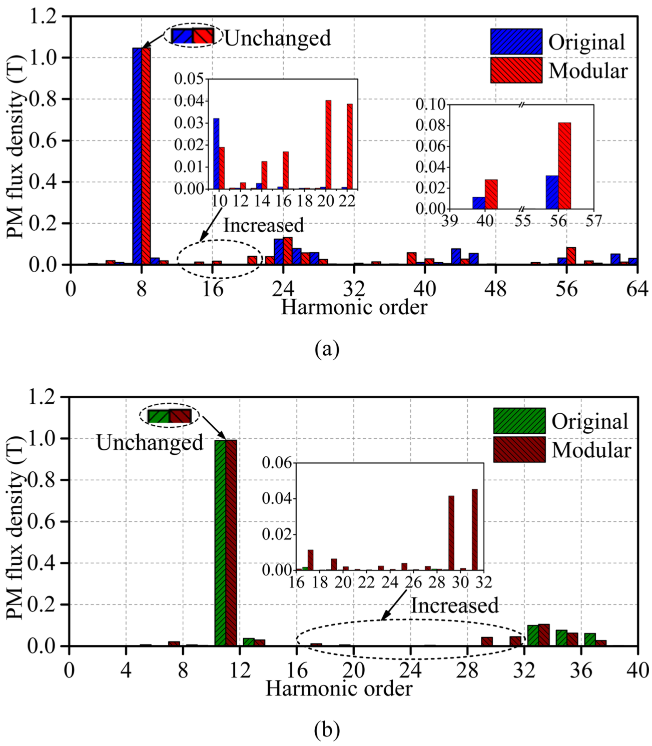

Fig. 9. (Color online) Harmonic spectrum comparison of PM magnetic field in PMGs with different slot/pole combinations. (a) 18-slot/16-pole. (b) 24-slot/22-pole.

Finally, Fig. 9 compares the harmonic spectrum of the permanent magnet field of the 18-slot/16-pole and 24-slot/22-pole PMGs for which the original and modular structures are adopted, respectively. Compared with the original structure, the modular structure has the same influence trend on the permanent magnet field. Taking the 18-slot/16-pole PMG as an example, the fundamental flux density amplitudes of the original and modular structures are both equal to 1.04 T. Namely, the fundamental component remains essentially unchanged. Besides, the modular structure increases the harmonic components of the permanent magnet field compared with the original structure, such as 12th-, 14th-, 16th-, 20th-, and 22nd-order harmonics. The newly generated harmonic components are less than 0.1 T, indicating relatively low amplitude. From the harmonic variation shown in Fig. 9(b), the harmonic characteristics of the 24-slot/22-pole generator can be derived, and redundant elaboration is omitted here.

3.2. Armature Field

Fig. 10 shows the winding functions of the 18-slot/16-pole PMG with the original and modular structures, respectively. The three-phase winding functions of both structures can be expressed as:

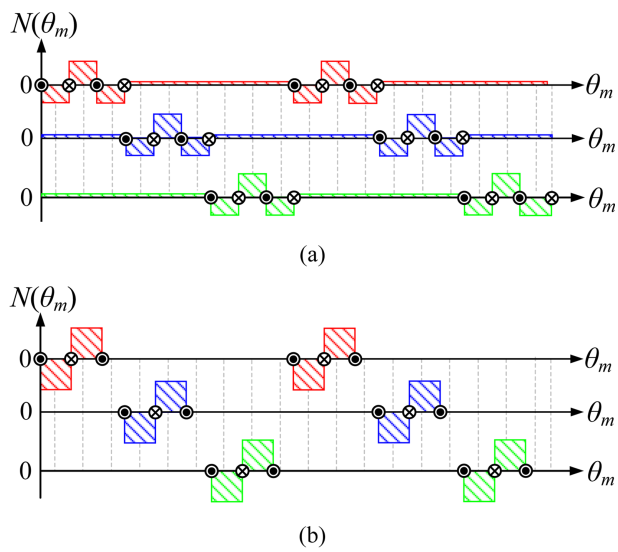

Fig. 10. (Color online) Winding function of the 18-slot 16-pole PMG. (a) Original. (b) Modular.

$$\begin{cases} N_{\mathrm{A}}(\theta_m) = \dfrac{2N_{\mathrm{ph}}k_{wv}}{v\pi} \cdot \displaystyle\sum_{v=1,2,3\ldots} \cos\left(v\theta_m + \beta_v\right) \\ N_{\mathrm{B}}(\theta_m) = \dfrac{2N_{\mathrm{ph}}k_{wv}}{v\pi} \cdot \displaystyle\sum_{v=1,2,3\ldots} \cos\left[v\left(\theta_m - \dfrac{4\pi}{3}\right) + \beta_v\right] \\ N_{\mathrm{C}}(\theta_m) = \dfrac{2N_{\mathrm{ph}}k_{wv}}{v\pi} \cdot \displaystyle\sum_{v=1,2,3\ldots} \cos\left[v\left(\theta_m - \dfrac{2\pi}{3}\right) + \beta_v\right] \end{cases} \tag{4}$$

where N_{ph} denotes the series number of turns per phase, β_v denotes the initial phase angle of the v^{th}-order harmonic of the Phase A winding function, and β_v=-90° or 90°. k_{wv} denotes the winding factor of the v^{th}-order harmonic, which can be calculated from the slot vector star diagrams shown in Figs. 11 and 12. Different from the original structure, the modular structure changes the spatial positions of the stator slots, leading to different spatial distributions of slot vectors and hence different winding factors for various harmonics [20], as listed in Table 2. Specifically, the fundamental winding factor increases from 0.945 to 1 for the modular structure, indicating the potential for higher torque density. Meanwhile, the winding factors of the 2nd-, 4th-, and 14th-order harmonics become larger, resulting in higher harmonic content, whereas the winding factor of the 10th-order tooth harmonic becomes smaller, leading to lower tooth harmonic content. Fig. 13 compares the harmonic spectrum of the armature field of the 18-slot/16-pole and 24-slot/22-pole PMGs with the original and modular structures. The modular structure effectively increases the amplitude of the fundamental component. Using the same analytical method, the winding factor table of the 24-slot/22-pole PMG with the original and modular structures can also be obtained and is omitted here for brevity. Then, the core losses of the 18-slot/16-pole and 24-slot/22-pole PMGs with different structures are compared in Fig. 14. The modular structure slightly increases the core loss due to the increment in MMF harmonic components.

Table 2. Winding factor of 18-slot/16-pole PMG with different stator structures.

Harmonic order	Original	Modular
2	0.061	0.271
4	0.140	0.707
8	0.945	1
10	0.945	0.653
14	0.140	0.271
16	0.061	0

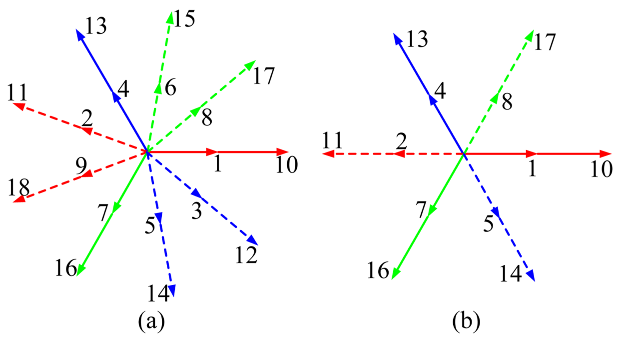

Fig. 11. (Color online) Slot vector star diagram of the 18-slot/16-pole PMG. (a) Original. (b) Modular.

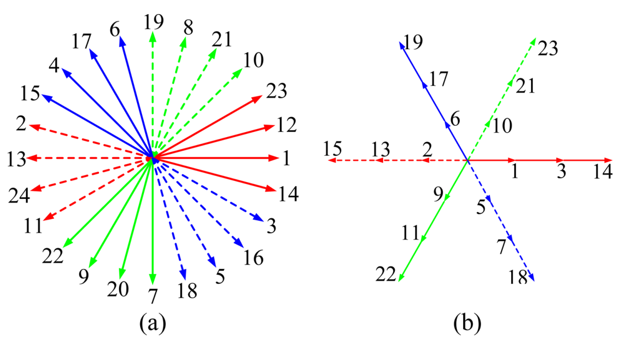

Fig. 12. (Color online) Slot vector star diagram of the 24-slot/22-pole PMG. (a) Original. (b) Modular.

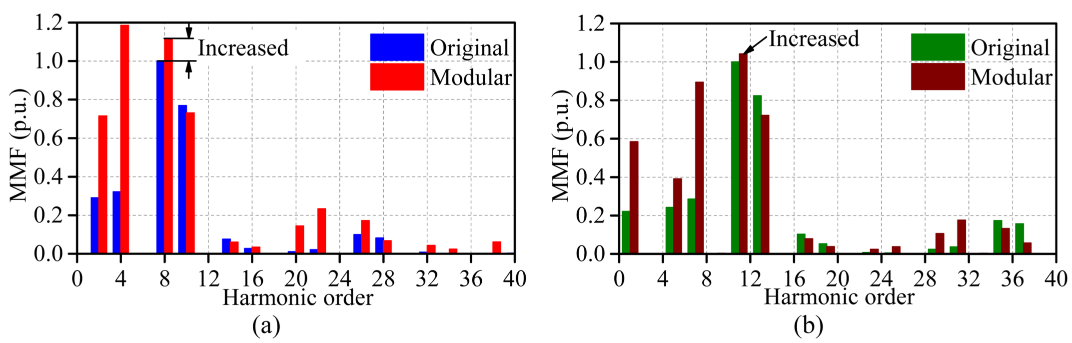

Fig. 13. (Color online) Harmonic spectrum comparison of MMF in PMGs with different slot/pole combinations. (a) 18-slot/16-pole. (b) 24-slot/22-pole.

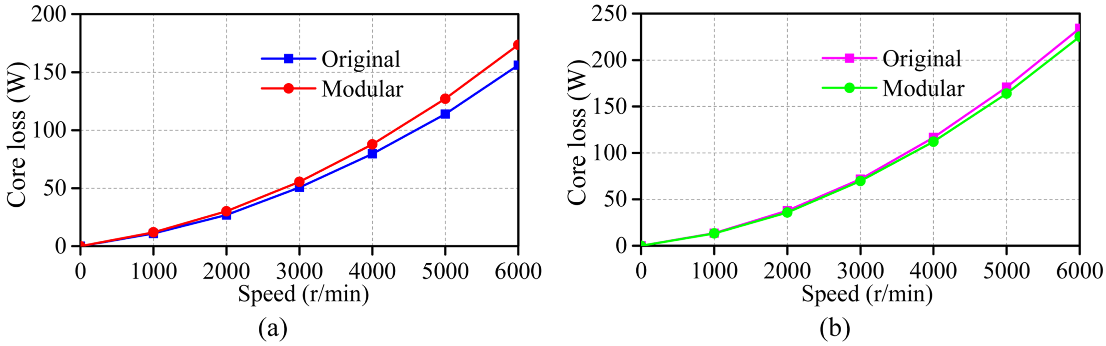

Fig. 14. (Color online) Comparison of core loss for PMGs with different slot/pole combinations. (a) 18-slot/16-pole. (b) 24-slot/22-pole.

4. Comparison of Electromagnetic Performance

4.1. Torque Comparison

According to the magnetic field analyses, the modular structure of the 18-slot/16-pole PMG does not sacrifice the fundamental amplitude of the permanent magnet field, while it increases the fundamental amplitude of the armature field. Therefore, the modular structure can effectively improve the average torque, as shown in Fig. 15(a). Using the same analytical approach, the modular structure can also improve the average electromagnetic torque of the 24-slot/22-pole permanent magnet generator. Besides, in the absence of stator modulation, the harmonic orders of the primitive PM flux density are 8^{th}-, 24^{th}-, 40^{th}-, 56^{th}-, etc. Based on Fig. 8, the primitive 8^{th}-order fundamental component is modulated to 40^{th}- and 56^{th}-order harmonics for the modular structure. The interaction between the primitive 40^{th}- and 56^{th}-order harmonics and the modulated 40^{th}- and 56^{th}-order harmonics is the main cause of cogging torque. As can be seen from Fig. 9(a), the modular structure increases the modulated 40^{th}- and 56^{th}-order harmonics, which leads to an increase in cogging torque. Consequently, the torque ripple of the electromagnetic torque is also aggravated to some extent, as shown in Fig. 15(b).

4.2 Inductance Comparison

The armature magnetomotive force is closely related to the inductance, and their relationship can be expressed as:

$$\begin{cases} L_{AA} = \dfrac{4\mu_0 R_g L_{ef} N_{ph}^2 \Lambda_{s0}}{\pi^2} \cdot \displaystyle\int_0^{2\pi} \sum_{v=1,3,5\ldots} \left(\dfrac{k_{wv}}{v} \cos\left(v\theta_m + \beta_v\right) \right)^2 d\theta_m \\ M_{AB} = \dfrac{4\mu_0 R_g L_{ef} N_{ph}^2 \Lambda_{s0}}{\pi^2} \cdot \displaystyle\int_0^{2\pi} \begin{matrix} \displaystyle\sum_{v=1,3,5\ldots} \left(\dfrac{k_{wv}}{v} \right)^2 \cos\left(v\theta_m + \beta_v\right) \\ \times \cos\left[v\left(\theta_m - \dfrac{4\pi}{3}\right) + \beta_v \right] \end{matrix} d\theta_m \end{cases} \quad (5)$$

where μ_0 is the permeability of vacuum, R_g is the radius of the air-gap, and L_{ef} is the stack length. For the 18-slot/16-pole PMG, the modular structure increases the harmonic content of the armature magnetomotive force, thus increasing the self-inductance. Besides, as can be seen from Fig. 10, there is substantial overlap among the winding functions of different phase windings in the original structure, whereas the winding functions of each phase are mutually independent with no overlapping

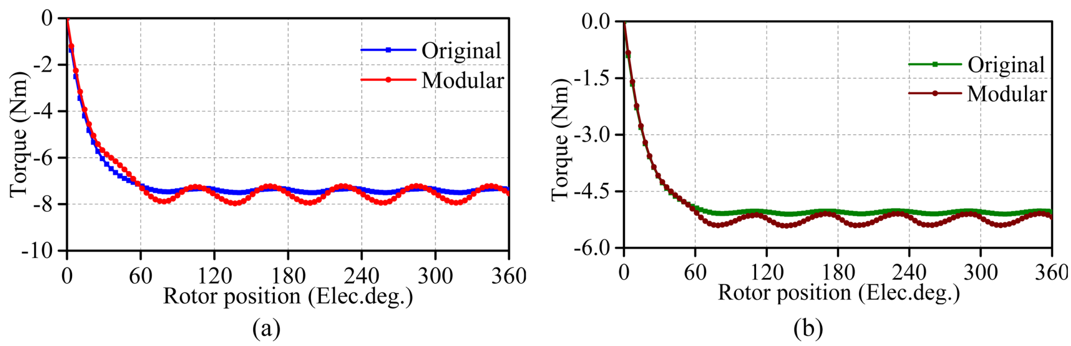

Fig. 15. (Color online) Comparison of torque curve for PMGs with different slot/pole combinations. (a) 18-slot/16-pole. (b) 24-slot/22-pole.

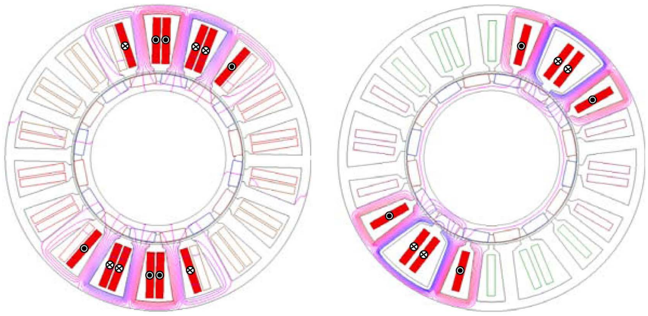

(a) (b)

Fig. 16. (Color online) Magnetic field distribution diagram of the 18-slot/16-pole PMG when only excited by phase A. (a) Original. (b) Modular.

region in the modular structure. Therefore, compared with the original structure, the magnetic fields produced by the armature winding in the modular structure are more independent, and the magnetic coupling region is smaller, as shown in Fig. 16. Consequently, the mutual inductances of the 18-slot/16-pole PMG with the modular structure are smaller, as shown in Fig. 17(a). The modular structure can also increase the self-inductance and reduce the mutual inductance of the 24-slot/22-pole PMG, as shown in Fig. 17(b).

Based on coordinate transformation, the relationship between the inductances in the ABC coordinate system and those in the d-q coordinate system can be expressed as:

$$\begin{cases} L_d \approx (L_0 - M_0) + (\frac{L_2}{2} + M_2) \\ L_q \approx (L_0 - M_0) - (\frac{L_2}{2} + M_2) \end{cases} \tag{6}$$

where L_0, L_2, L_4, and L_8 denote the corresponding harmonic components of self-inductance, while M_0, M_2, M_4, and M_8 denote the corresponding harmonic compo-

Table 3. Inductance component of PMGs with different slot/pole combinations.

Items	18-slot/16-pole		24-slot/22-pole	
	Original	Modular	Original	Modular
L_0 (mH)	4.77	7.17	4.11	5.47
L_2 (mH)	-0.19	-0.25	-0.10	-0.08
M_0 (mH)	-0.37	0.03	-0.22	0.02
M_2 (mH)	-0.03	-0.04	-0.01	-0.03

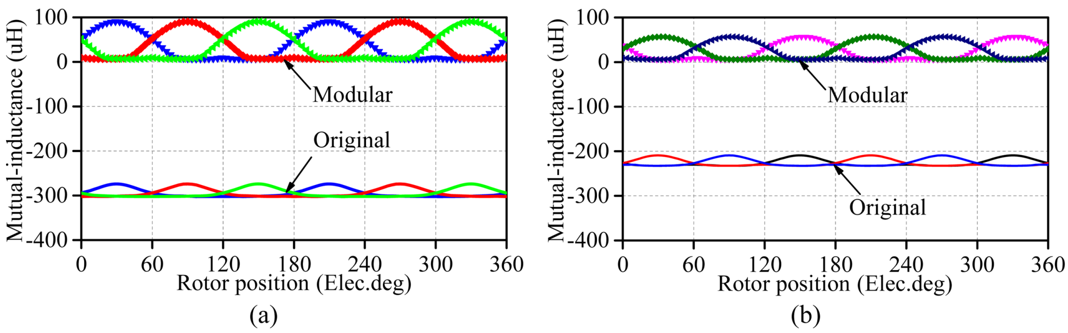

Fig. 17. (Color online) Comparison of mutual-inductance curves of PMGs with different slot/pole combinations. (a) 18-slot/16-pole. (b) 24-slot/22-pole.

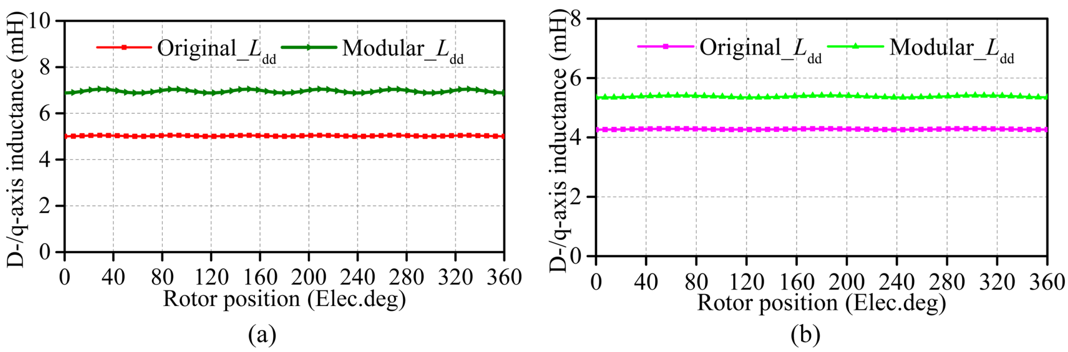

Fig. 18. (Color online) Comparison of d- and q-axis inductances of PMGs with different slot/pole combinations. (a) 18-slot/16-pole. (b) 24-slot/22-pole.

nents of mutual inductance. The amplitudes of these inductance components are listed in Table 3. Furthermore, Fig. 18 compares the d-axis and q-axis inductance curves of the 18-slot/16-pole and 24-slot/22-pole PMGs with different structures. Owing to the significant increase in the average component of self-inductance, the modular structure has greater q-axis inductance than the original structure, and the improvement is more pronounced for the 18-slot/16-pole PMG.

4.3. Comparison of Short-Circuit Current

Under a three-phase short-circuit fault, the q-axis and d-axis terminal voltages can be expressed as [21]:

$$\begin{cases} Ri_d(t) - \omega_e L_q i_q(t) + L_d \dfrac{d\left[i_d(t)\right]}{dt} = 0 \\ Ri_q(t) + \omega_e L_d i_d(t) + \omega_e \psi_{\mathrm{PM}} + L_q \dfrac{d\left[i_q(t)\right]}{dt} = 0 \end{cases} \tag{7}$$

where R denotes phase resistance, ω_e is electrical angular velocity, t is time, Ψ_{PM} is permanent magnet flux linkage, i_d and i_q are the d-axis and q-axis currents, respectively, and L_d and L_q are the d-axis and q-axis inductances. For surface-mounted permanent magnet generators, L_d=L_q. By applying the Laplace transform and inverse transform to the above equations, the expressions for the d-axis and q-axis currents under a three-phase short-circuit fault can finally be obtained as:

$$\begin{cases} i_d(t) = -\dfrac{L_d \omega_e^2 \psi_{\mathrm{PM}}}{(\omega_e L_d)^2 + R^2}\left[1 - \dfrac{1}{\sin\zeta} e^{-\frac{R}{L_d}t} \sin(\omega_e t + \zeta)\right] \\ i_q(t) = -\dfrac{R\omega_e \psi_{\mathrm{PM}}}{(\omega_e L_q)^2 + R^2}\left[1 - \dfrac{1}{\cos\zeta} e^{-\frac{R}{L_q}t} \cos(\omega_e t + \zeta)\right] \end{cases} \tag{8}$$

where ζ=arctan($\omega_e L_q/R$). The SCC consists of transient and steady-state components. As the rotational speed increases, the reactance becomes much greater than the resistance. That is, $\omega_e L_q \gg R$. The d-axis SCC can thus be expressed as:

$$i_d(t) = -\frac{\psi_{\mathrm{PM}}}{L_d} \tag{9}$$

As can be seen from Fig. 9, the adoption of the stator structure does not affect the permanent magnet field. Therefore, the permanent magnet flux linkage is the same under different structures. It follows that increasing of the d-axis inductance is an effective method for suppressing SCC. Namely, the larger the d-axis inductance is, the smaller the SCC is.

Fig. 19 compares the current trajectory of different structures under three-phase short-circuit fault. When three-phase short-circuit fault occurs in the 18-slot/16-pole PMG, the maximum d-axis currents of the original and modular structures are -47.0 A and -34.2 A, respectively, corresponding to a reduction of 27%. By contrast, for the 24-slot/22-pole PMG under three-phase short-circuit fault, the maximum d-axis currents of the original and modular structures are -35.4 A and -30.8 A, respectively, corresponding to a reduction of 13%. It can be seen that the modular structure has a more significant SCC suppression effect for the 18-slot/16-pole PMG.

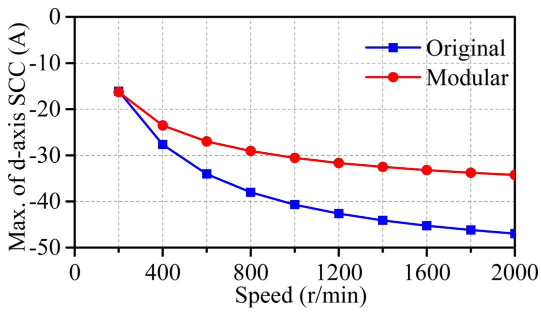

Fig. 20. (Color online) Maximum d-axis SCC curve of the 18-slot/16-pole PMG varying with rotational speed.

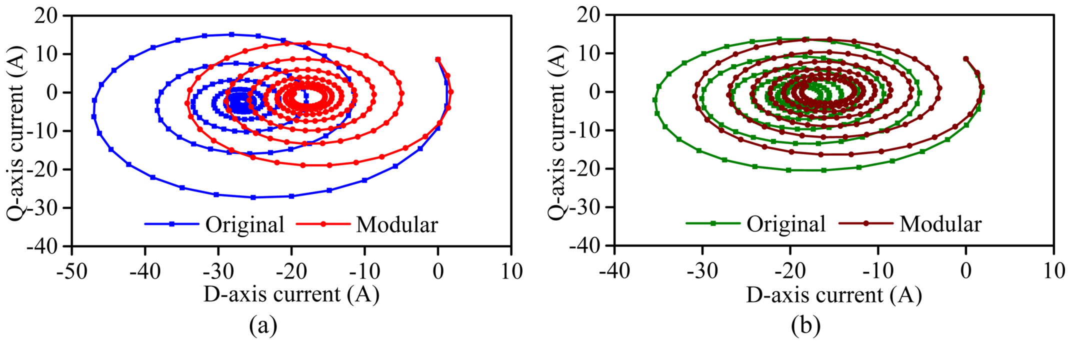

Fig. 19. (Color online) Short-circuit current trajectory of PMGs with different slot/pole combinations at 2000 r/min. (a) 18-slot/16-pole. (b) 24-slot/22-pole.

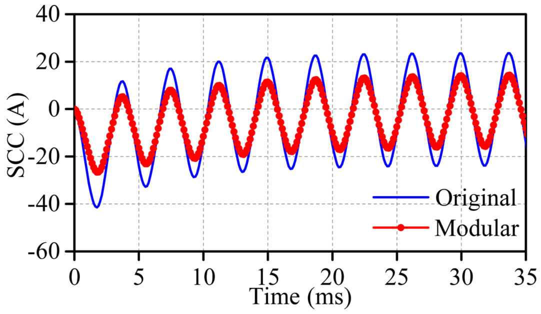

Fig. 21. (Color online) SCC curve of the 18-slot/16-pole PMG with phase A fault at 2000 r/min.

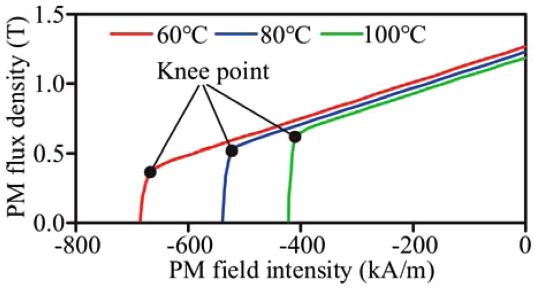

Fig. 22. (Color online) The demagnetization curves of N42 under different temperatures.

Furthermore, Fig. 20 compares the variation of the maximum d-axis SCC of the 18-slot/16-pole PMG with speed. As the speed increases, the suppressing effect of the modular structure on the d-axis SCC becomes more pronounced.

In addition, when the single-phase short-circuit fault occurs in the 18-slot/16-pole PMG, Fig. 21 compares the

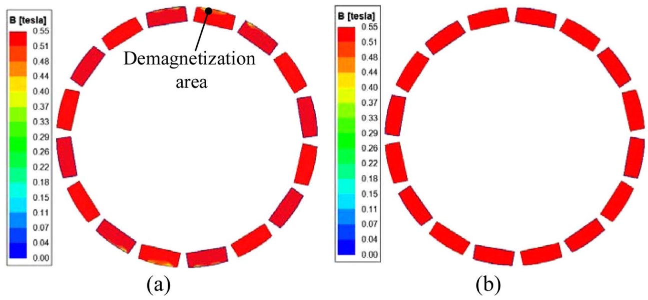

Fig. 23. (Color online) The demagnetization cloud diagrams of the 18-slot/16-pole PMG with different structures at 4000 r/min. (a) Original. (b) Modular.

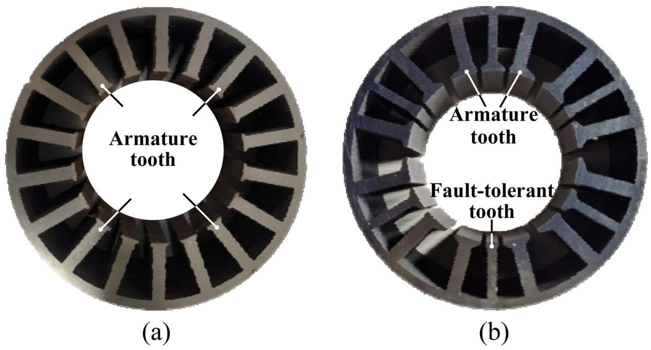

Fig. 24. (Color online) Stator structure of the 18-slot/16-pole PMG prototype. (a) Original. (b) Modular.

single-phase SCC curves of different structures at 2,000 r/min. In the original structure, the maximum and steady-state short-circuit currents are 41.5 A and 23.6 A, respectively, whereas they are 26.6 A and 14.5 A, respectively, in the modular structure. Fig. 22 shows the demagneti-

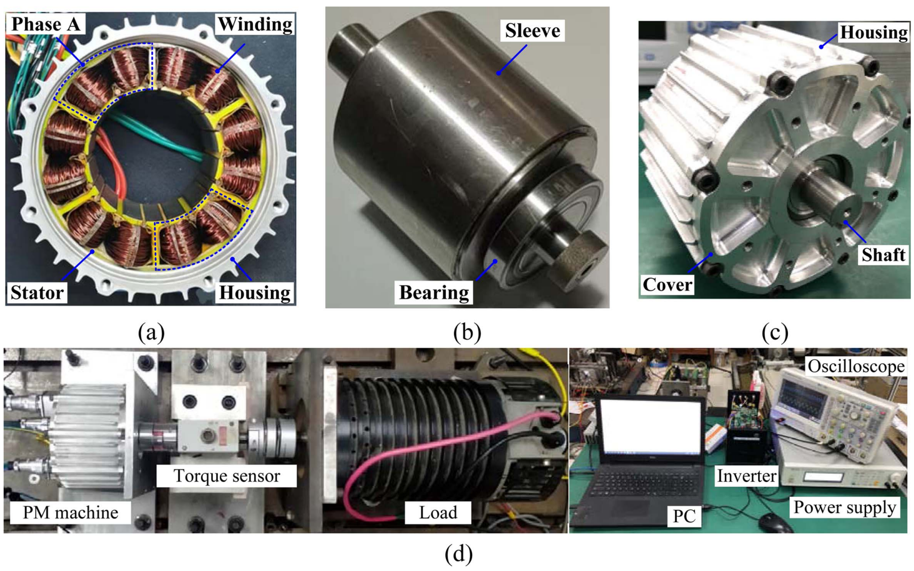

Fig. 25. (Color online) Prototype components and testing platform. (a) Stator. (b) Rotor. (c) Assembly. (d) Testing platform.

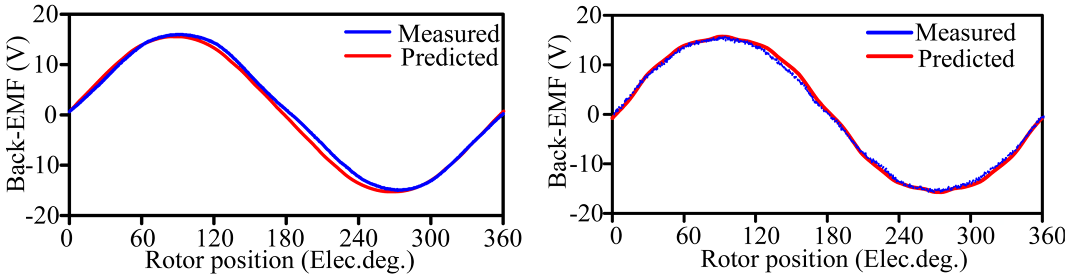

(a) (b)

Fig. 26. (Color online) Comparison of the measured and predicted back-EMF curves of the 18-slot/16-pole PM machine prototype. (a) Original. (b) Modular.

zation curves of N42 at different temperatures, and the knee point is 0.55 T when the temperature reaches 100 °C. This material is utilized in the PMG studied in this paper. Then, the demagnetization cloud diagrams of 18-slot/16-pole PMG with different structures at 4,000 r/min are compared in Fig. 23. The original structure has already exhibited demagnetization areas, whereas the modular structure almost has no demagnetization area.

5. Experimental Validation

To verify the effectiveness of the proposed modular stator structure in improving performance, prototypes of the 18-slot/16-pole PMGs with the original and modular structures were manufactured, as shown in Fig. 24. The experimental test platform was built for both machines, as shown in Fig. 25. Fig. 26 shows the no-load back-EMF curves of the prototypes with different structures at 200 r/min. The measured curves agree well with the predicted curves, indicating high machining accuracy of the prototypes. Furthermore, the self-inductance curves of the prototypes with the original and modular structures were measured using TH2811D LCR digital bridge, as shown in Fig. 27. Consistent with the theoretical analysis, the prototype with the modular structure exhibits a larger average self-inductance than the original one.

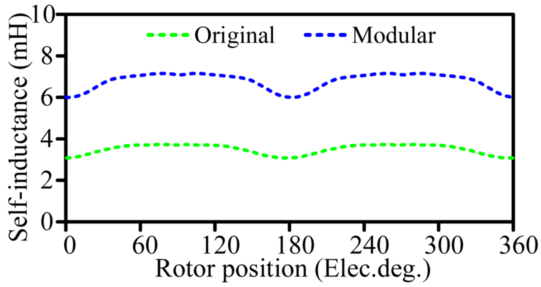

Fig. 27. (Color online) Self-inductance measured curve of the 18-slot/16-pole PM machine prototype with different structures.

Fig. 28 shows the measured torque curves of the prototypes with the original and modular structures, and the phase current amplitude is at the rated value of 7 A in both cases. The average torques of the original and modular structures are 7.5 Nm and 7.9 Nm, respectively. The modular structure has a larger average torque, verifying the correctness of the theoretical analysis. To validate the effectiveness of the proposed modular structure in suppressing SCC, the positive and negative

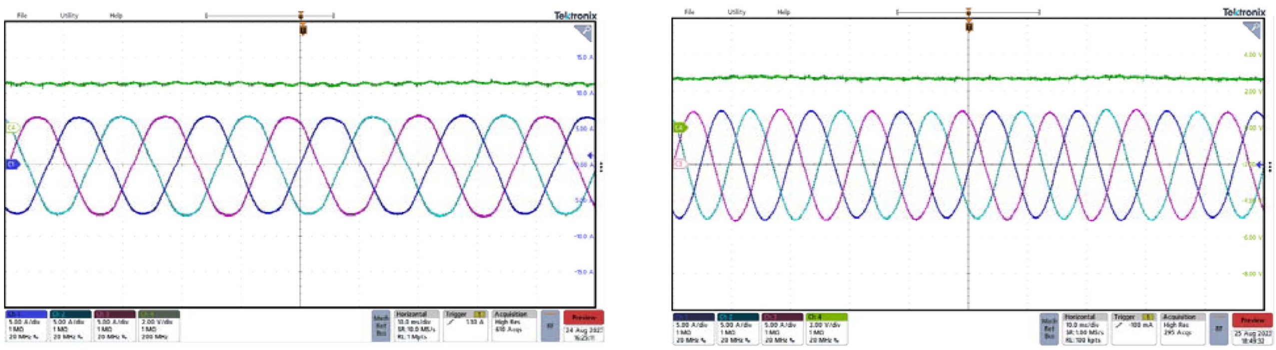

(a) (b)

Fig. 28. (Color online) Measured torque curves of the 18-slot/16-pole PM machine prototype. (a) Original. (b) Modular.

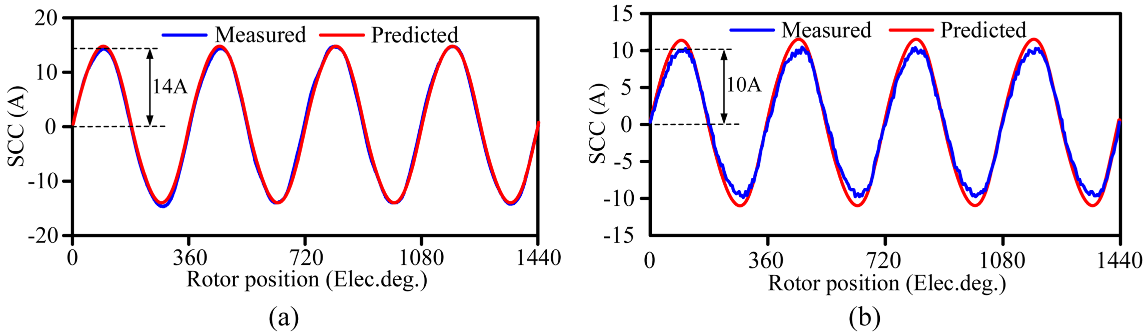

Fig. 29. (Color online) Comparison of measured and predicted SCC curves of the 18-slot/16-pole PM machine prototype with phase A short-circuit fault. (a) Original. (b) Modular.

terminals of Phase A were shorted together to simulate a single-phase short-circuit fault. Namely, the fault type studied in this paper is a line-to-neutral fault. Then, the two prototypes were driven by a DC motor to the same specified speed. The SCC curves were measured using a current clamp, as shown in Fig. 29. On the one hand, the SCC amplitudes of the original and modular structures were 14 A and 10 A, respectively, indicating a reduction of 28.6% under the modular structure. On the other hand, the measured SCC curves agree well with the predicted curves, thus verifying the correctness of the theoretical analysis.

6. Conclusion

To meet the application requirements of wind generators for high reliability and high torque density, a modular concentrated winding structure based on stator tooth offset was proposed. This structure effectively reduces the SCC while enhancing its average torque. The characteristics of the modular concentrated winding structure were described in detail, and the evolution law from the original structure to the modular structure was summarized. Then, the influence of the modular structure on magnetic field harmonic content was analyzed according to the magnetic field modulation theory. Analysis results show that the modular structure preserves the fundamental component of the permanent magnet field while increasing the fundamental amplitude of the armature field. After that, the impacts of the modular structure on electromagnetic performance were analyzed under both normal and short-circuit conditions. For the 18-slot/16-pole PMG, under normal operation, the average torque increased by 3.0% and the mutual inductance amplitude decreased by 91.9 %, while the SCC was reduced by 28.6% under short-circuit fault conditions. Finally, an 18-slot/16-pole prototype was developed and experimentally tested. The experimental results show good agreement between the measured and predicted results, thus verifying the effectiveness of the proposed modular concentrated winding structure.

Acknowledgment

This work was supported by the Open Research Fund of Jiangsu Collaborative Innovation Center for Smart Distribution Network, Nanjing Institute of Technology (XTCX202501).

References

[1] P. N. Harmony, J. Park, and J. Baek, J. Magn. **30**, 345 (2025).
[2] J. Seo, J. Magn. **27**, 147 (2022).
[3] K. Lee and S. Lee, J. Magn. **30**, 688 (2025).
[4] H. Chen, Y. Zhang, C. Yang, and T. Jiang, IEEE Trans. Ind. Electron. **73**, 1690 (2026).
[5] M. M. Tezcan and C. Yesildag, 2025 International Conference on Electromechanical and Energy Systems (SIELMEN), Iasi, Romania, 130 (2025).
[6] L. Xie, T. Liu, Y. Li, P. Su, and G. Zhao, J. Magn. **30**, 307 (2025).
[7] X. Tang, G. Zhang, W. Huo, and Q. Zhang, J. Magn. **30**, 374 (2025).
[8] J. Mao, X. Xu, Y. Tang, Y. Ren, J. Feng, and J. Zheng, J. Magn. **30**, 266 (2025).
[9] L. Miao, M. Xu, and Q. Zhang, J. Magn. **29**, 397 (2024).
[10] Y. Sun, W. Zhao, J. Ji, N. Bianchi, and Y. Zhou, IEEE Trans. Energy Convers. **40**, 2423 (2025).
[11] Y. Sun, W. Zhao, J. Ji, J. Zheng, and X. Song, IEEE Trans. Ind. Electron. **69**, 1135 (2022).
[12] J. Park, P. N. Harmony, and J. Baek, J. Magn. **30**, 596 (2025).
[13] G. Xu, P. Hu, Z. Li, H. Zhao, and Y. Zhan, IEEE Trans. Ind. Appl. **58**, 7171 (2022).
[14] Y. Du, L. Wu, H. Zhan, and Y. Fang, IEEE Trans. Energy Convers. **36**, 2514 (2021).

[15] Y. Sun, Z. Wang, H. Wei, B. Yuan, and X. Wang, J. Magn. **29**, 387 (2024).
[16] G. Li, B. Ren, Z. Q. Zhu, M. P. Foster, and D. A. Stone, IEEE Trans. Ind. Appl. **54**, 1302 (2018).
[17] Y. Cheng, Z. Wang, and D. Li, J. Magn., **24**, 506 (2019).
[18] P. Sun, S. Jia, D. Liang, and R. Qu, IEEE Trans. Transp. Electrific. **10**, 7374 (2024).
[19] B. Wang, Y. Wang, Z. Zhang, M. Tang, G. Vakil, and T. Yang, Chin. J. Electr. Engin. **11**, 165 (2025).
[20] H. Xu, J. Huang, X. Xu, and J. Zheng, J. Magn. **28**, 258 (2023).
[21] P. Xu, J. Feng, S. Guo, S. Feng, W. Chu, Y. Ren, and Z. Q. Zhu, IEEE Trans. Ind. Electron. **65**, 1941 (2018).